Voltage gated inter-cation selective ion channels from graphene nanopores

Lauren Cantley[a], Jacob L. Swett[b], David Lloyd[a], David A. Cullen[c], Ke Zhou[d], Peter V. Bedworth[b], Scott Heise[b], Adam J. Rondinone[e], Zhiping Xu[d], Steve Sinton[b], J. Scott Bunch[a,f]*

Methods:

Device Fabrication. 200 nm thick low-stress silicon nitride windows were patterned using standard photolithography followed by an anisotropic KOH etch of the underlying silicon. A 3-5 µm diameter through hole was patterned in the center of the silicon nitride window via reactive ion etching (RIE) using an SF_6-Ar plasma. 20 nm of ALD Al_2O_3 was deposited, conformally coating the support chip. After a pre-synthesis anneal of the Cu foil substrate, CVD graphene was grown via low-pressure CVD. Following synthesis, the graphene, while still on the Cu foil substrate, was irradiated with 500 eV Xe^+ ions for a total fluence of 3.7 x 10^{13} Xe^+/cm^2. This process has been shown to not introduce visible >nm hole defects when analyzed by STEM. The Cu foil substrate was then etched away with ammonium persulfate and the CVD graphene was transferred, without a sacrificial carrier layer, over the 5 µm through hole in the silicon nitride window. Once transferred, the graphene was exposed to 180 seconds of UVO to reduce hydrocarbon surface contamination. Through STEM imaging, this was confirmed not to introduce defects into the single-layer graphene itself. The gate electrode was defined via shadow mask lithography to be in

contact with the graphene and 5 nm chromium followed by 60 nm gold were deposited via thermal evaporation.

CVD graphene samples were perforated via site specific focused helium ion drilling. For HIM drilling, pores were drilled using a Zeiss ORION NanoFab scanning HIM equipped with a gas field ion source (GFIS) using He^+ ions at 25 kV. Small pores were drilled with a stationary beam in defined locations with a beam current of 0.5-2.0 pA, and a dwell time of 52 ms per pore. Larger pores were drilled by defining a pattern and dwelling the beam with a 1 nm pixel spacing over that region with a dose on the order of 1 $nC/\mu m^2$ ($1x10^{18}$ He^+/cm^2).

I-V and conductance measurements. Conductance measurements were carried out in a custom made microfluidic cell fabricated via standard PDMS soft lithography. The structure allowed for electrolyte solution to be introduced to both sides of the membrane, while still allowing for AFM access to the top side of the membrane. Two microchannels, 50 µm tall and 2000 µm wide, were patterned into PDMS and bonded to a glass slide. Four inlet ports are punched into the PDMS, with the graphene on silicon nitride chip mounted over the center ports that connect the two underlying microchannels. PDMS was painted over the edge of the chip to create a seal and isolate volumes on either side of the chip. The device was dried for 2 days at room temperature to allow the PDMS seal to cure.

Graphene membranes were first rinsed with ethanol for 2 minutes followed by deionized water to facilitate wetting of the nitride membrane. Once graphene devices were introduced to fluid, membranes remained in solution for the duration of the experiments. Devices were exposed to electrolyte solution for 5-10 minutes before conductance measurements were carried out. Solutions were left unbuffered to avoid any potential interactions between the graphene and solutes. For the duration of the experiments, all solution pHs ranged from 5.91 – 6.38. To change the electrolyte solution, the microfluidic cell was first flushed with deionized water for 8 minutes, and then the new electrolyte was introduced. To ensure the observed selectivity was not an artifact of switching

between solutions, the order in which different salt solutions were measured was varied, and we repeatedly alternated back and forth between salt solutions to confirm the differences in conductance were stable.

If a device did not display appreciable conductance upon initial wetting, it was exposed to ethanol for additional time. The I-V curves used for selectivity measurements within the text correspond to when a device was first witnessed to have appreciable conductance in aqueous solution. For extended storage, devices were stored in either deionized water or 0.1M KCl at 4° C.

I-V characteristics were measured with a DL Instruments model 1211 current preamplifier with silver/silver chloride electrodes at a sampling speed ranging from $1 - 10$ mV/s. The voltage was ramped up and back down for each I-V measurement.

In order to measure selectivity, the concentrations used to measure conductance were chosen to maintain a constant chloride ion concentration across experiments comparing both monovalent and divalent ions; for example a 100 mM concentration for monovalent ions and a 50 mM concentration for divalent ions. This ensured that differences in conductance were due to differences in ion mobility and not from differences in bulk conductivity. Conductance values in the main text were determined by taking a linear fit of the IV curve for +/- 50 mV around $V_s = 0$ mV, unless otherwise noted.

Bulk conductivities of the solutions used in this study were measured using Mettler Toledo S230 SevenCompact^{TM} conductivity meter with InLab$^{®}$ 731 ISM probe for concentrations $\geq 10^{-2}$ M and InLab$^{®}$ 741 ISM probe for concentrations $< 10^{-2}$ M.

Imaging. Aberration-corrected STEM imaged graphene devices were imaged in a Nion UltraSTEM 100 operated at 60 kV. Prior to imaging, the devices were baked at 160° C for 6-8 hours in a vacuum chamber to remove mobile hydrocarbon contamination. Aberration-corrected STEM images were acquired using a medium-angle annular dark-field (MAADF) detector with a

54-200 mrad collection semi-angle. A convergence semi-angle of 30 mrad and probe current of 60-80 pA was used to acquire atomic resolution images of the pore edges.

HIM imaged graphene devices were imaged in a Zeiss ORION NanoFab operated at 25 kV with He$^+$. No special preparation was performed prior to drilling and imaging. To limit the ion dose to the samples, images were acquired at a large field of view relative to the pores (typically 5 x 5 µm), with beam currents between 0.5-2.0 pA, 512x512 resolution, and 2-50 µs dwell time per pixel.

AFM images were taken with an Asylum MFP-3D microscope operated in tapping mode. Platinum-iridium coated silicon AFM tips (ARROW-NCPt) were used for air imaging. For fluid imaging, Si_3N_4 tips (PNP-TR, spring constant k_c= 0.32 N/m) were driven at a free air amplitude of around 50 nm. After tip engagement, the set point amplitude was adjusted to be as high as possible, set just below the value at which the tip lost contact with the surface. This meant the tip would exert the smallest possible forces and avoid modifying the topology of the sample being measuring. Scanning speeds were approximately 3 µm/s, and post-processing of the images was carried out to remove low frequency noise.

Molecular Dynamics Simulations. We perform MD simulations using the large-scale atomic/molecular massively parallel simulator (LAMMPS)[1]. A quasi-two-dimensional pore-bubble model is constructed with a thickness of 2.91 nm along the z direction (Figure 3e) to minimize the size effect in the MD simulations[2]. The all-atom optimized potentials for liquid simulations[3] are used for the graphene. The SPC/E model is used for water, which is widely adopted for MD simulations of water transport as it predicts reasonable static and dynamic propensities[4]. The van der Waals interactions between water and the nanoporous graphene membrane are modeled in the Lennard-Jones (L-J) 12-6 form, *i.e.* $V = 4\varepsilon[(\sigma/r)^{12} - (\sigma/r)^6]$. The zigzag edge of graphene is terminated by hydrophilic carbonyl groups with a density of one group per under-coordinated carbon atoms, following the experimental evidence[5]. The interaction between carbon atoms in graphene or GO and oxygen atoms in water is modeled with parameters

$\varepsilon_{C-O} = 4.063$ meV and $\sigma_{C-O} = 0.319$ nm. This set of parameters predicts a water contact angle of 98.4° for graphene, consistent with the value measured experimentally[6]. For the ions, we use the force-field parameters developed by Kenneth's group, listed in Table S1, which are optimized for a reliable description of the free energy and shell structure of ion solvation, with long-range electrostatic interactions treated by using the particle-mesh-Ewald (PME) method[3]. A Weeks-Chandler-Andersen (WCA) gas model[4] is used to simulate the bubble, with interatomic interaction described using a 12-6 L-J potentials ($\varepsilon = 0.0103$ eV, $\sigma = 0.34$ nm), truncated and shifted at interatomic distance $r = 2^{1/6}\sigma$. Hetero-atomic parameters for the 12-6 L-J interactions are determined through the Lorentz-Berthelot mixing rules.

The translocation pathway and PMF of ion transport along paths **1** and **2** (Figure 4a) are determined by umbrella sampling (US)[5]. We use a harmonic-spring biasing to constrain the ionic position at a specific value of d (Figure S1a). For path **1** in the film and the fully-immersed model models (model 1 and 2 in Figure S1a), the force constant is set to 10^4 and 10^3 kJ/mol/nm^2 for $d = 0.20$-0.35 nm (0.05 nm per window) and $d = 0.4$-1.0 nm (0.10 nm per window), respectively. For path **2**, a force constant of 2×10^3 kJ/mol/nm^2 is used (0.10 nm per window). Every window runs in a separate simulation for 6 ns and the trajectories are collected every 250 ps. The distribution of atomic positions in adjacent windows significantly overlaps. Finally, the PMF is generated by recombining individually-biased distributions using the weighted histogram analysis method[5], by using the package implementing by Grossfield[7]. The PMF profiles for path 1 (models 1 and 2) and path 2, using Na$^+$ as an example without the loss of generality, are shown in Figure S1b. For model 1 and model 2, the two distinct valleys correspond to the condition that the 1st/2nd HS is perturbed by the functionalized graphene edge (Figure S1c). The free energy barrier for translocation in model 2 is 2.0/1.0k_BT, respectively, close to the values measured in model 1 (1.9/0.8 k_BT).

The hydration radii of ions confined within thin water films are calculated following our previous work[8], by using a model with a 1-2.5 nm-thick water film on graphene (model 3 in Figure S1).

Control Measurements. Several control experiments were carried out to verify that the measured current was passing through the graphene pore(s) and not leaking through the graphene/silicon nitride interface or elsewhere. The following control devices were measured:

(1) ALD alumina coated silicon nitride membrane with no through-hole, no graphene. Isolate transport through silicon nitride membrane and through the PDMS sealing the device within microfluidic cell.

(2) ALD alumina coated silicon nitride membrane with 5 μm through-hole, no graphene. Determine limiting conductance for nitride through-hole.

(3) ALD alumina coated silicon nitride membrane with 5 μm through-hole, suspended unperforated CVD graphene.

Leakage conductance was measured to be less than 55 pS in 0.1 M KCl and less than 140 pS in 1.0 M KCl for type (1) control devices. The limiting conductance through type (2) control devices was measured to be on the order of μS for 0.1M KCl. For type (3) control devices, the conductance was less than 60 pS in 0.1M KCl and less than 280 pS in 1.0 M KCl.

Asymmetric ion conditions. In the main text, we concluded that cations were the majority charge carriers due to the selective I-V behavior and p-type gating behavior. However,

there is also the distinct possibility that the current is carried by anions, but modulated by cations. To address this we carried out conductance measurements with asymmetric ion conditions: 0.05 M CaCl$_2$ on one side of the membrane and 0.1 M KCl on the other. Concentrations were chosen to maintain a constant chloride concentration. In this configuration, we observed highly rectified behavior, consistent with the conclusion of cations as the majority charge carriers (Fig. S2).

Pore Termination. High magnification aberration-corrected STEM imaging was carried out to reveal the pore geometry, edge structure, and the surface of the graphene (Fig. S3). Carbon was the most prevalent edge termination in the pores imaged, however hydrocarbon contamination, which is prevalent across the surface of the graphene, was also present near the pore edges for several of the devices that were imaged.

Evidence for the presence of a bubble. We found further evidence for the presence of a bubble occluding the pore by varying tip-sample forces during scanning[9]. This was done by reducing the amplitude set point ratio (the ratio between the amplitude set point and the free air amplitude), which increases the forces on the sample from the tip. Figure S4 shows the result of imaging the pore in water with different set points ratios. The lower set point ratio of 30% caused the tip to deform the object over the pore (Fig. S4B) as compared with images using higher set point ratios of 36% (Fig. S4A). This means the object is soft and malleable, and has a similar response to AFM probing as seen in PDMS nanodroplets or gaseous nanobubbles[10]. During the subsequent scan the set point was raised again causing the tip-sample forces to reduce (Fig. S4C), and the bubble topology returned to the same state as before.

Conductance measurements in solvents of varying surface tensions. We performed

liquid AFM imaging on the device in two solvents with different surface tension: water

(72.86 mJ/m^2)[11] and ethanol (22.39 mJ/m^2)[12]. For the device shown in figure 1c, liquid

AFM imaging revealed that the surface nanobubble occluding the pore in aqueous solution

(Fig. S5A) was absent in ethanol (Fig. S5B), and returned when the solvent was exchanged

back to water (Fig. S5C). The device was not dried out and remained continuously wet

between solvent exchanges.

Additionally, Li$^+$ transport across three devices was measured in both aqueous and

ethanol based solutions. Bulk conductivities were measured to be 10.7 mS/cm for aqueous

0.1 M LiCl and 1.54 mS/cm for the ethanol based 0.1 M LiCl. Measurements are carried

out in the order shown in the legend, seamless switching between ethanol and aqueous

based LiCl solutions to keep the device wet at all times. Devices demonstrate increased

conductance across the pore for ethanol based solution when compared to aqueous solution

of the same ionic concentration. (Fig. S6A-C). The bulk conductivity of 0.1M LiCl in

ethanol is considerably less than 0.1M LiCl in H_20[11,12]. Thus, one would not expect the

conductance across the graphene pore to be greater in the ethanol solution unless the

transport pathway changed between the two measurements. This change in transport

pathway is due to the presence and absence of a nanobubble, witnessed via liquid AFM

imaging (Figure S4).

In situ measurements were also carried out to allow for monitoring of the conductance

while switching between ethanol and water solutions (Figure S6D). Sweeping the bias

voltage, the device was first measured in 0.1M LiCl in H_2O (blue arrow) and demonstrated

little conductance. As 0.1M LiCl in ethanol was introduced and the aqueous solution

flushed out, the conductance increased (orange arrow) and stayed at the elevated conductance level while the ethanol solution was present (green arrow). All the while, the voltage was continually swept, down to -500 mV and back to +500 mV. When the water solution was reintroduced and the ethanol solution flushed out, the conductance returned to the lower conductance state (purple arrow) and remained low while water solution was present (yellow arrow). This result was consistent with measurements in figure S6A-C.

AFM and conductivity measurements of a non-occluded pore. We performed conductivity and in-situ AFM measurements of nanopores which were not occluded. Figure S7A shows an AFM image of a HIM drilled nanopore imaged in water. The phase channel was used to plot the image in order to highlight regions of rapid change in the topology of the surface – in this case the edge of the nanopore (Fig. S7C). Immediately prior to AFM imaging, I-V curves of LiCl, NaCl and $CaCl_2$ solutions all demonstrated linear conductance (Fig. S8). We can estimate the nanopore diameter, d, which should give rise to a conductance G_i for each salt species i by using the theory for ion transport through a cylindrical pore, which yields the formula:

$$G_i = \sigma_i d \qquad\qquad (S1)$$

where σ_i is the bulk conductivity, and access resistance is assumed to be the dominant term[13]. Using values for G_i calculated from Fig. S7 and values for σ_i measured prior conductance measurements, Eq. S1 was used to calculate the predicted pore diameter d for each salt and tabulate the results in Table S2.

The pore conductivities for three different salts give consistent predictions for a pore size of ~75 nm in diameter. Comparing this prediction with the pore size measured with AFM in Fig. S7B, we see there is close agreement between the two. This confirms that when no occlusion is present over the pore, the observed nanopore conductance is consistent with the behavior we would expect for an infinitely thin cylindrical pore of that diameter.

Prevalence and formation of nanobubbles. To estimate the prevalence of nanobubbles in our experiments, we imaged six devices in water with AFM. We found the presence of nanobubbles in all six devices, four of which are shown in Fig. S10 as an example. Nanobubbles are distributed across the devices and are of various sizes. We found evidence of bubbles occluding the graphene nanopore in four of the six devices measured. The ethanol and water solutions were degassed in a vacuum desiccator for ~1h prior to measurement in three of these devices. In addition, we found that pores frequently had a conductance lower than is predicted analytically, given the imaged diameter of the pore. We interpret this as indirect evidence that the pore was obstructed due to bubble formation. We measured the pore diameter and conductance of aqueous salt solutions across 35 devices, including the nine devices highlighted in the main text, only two devices displayed a conductance magnitude consistent with what is predicted analytically for the imaged pore size. The other 33 devices all displayed lower than expected conductance values.

We hypothesize that the presence of hydrocarbon contamination around the pore mouth makes the pore region more hydrophobic, and therefore more prone to dewetting. This hydrocarbon contamination can be seen in Fig S11 which shows a HIM image of a device after pore milling. The bright regions around the pore are caused by charging of the electrically insulating hydrocarbons stuck to the graphene surface.
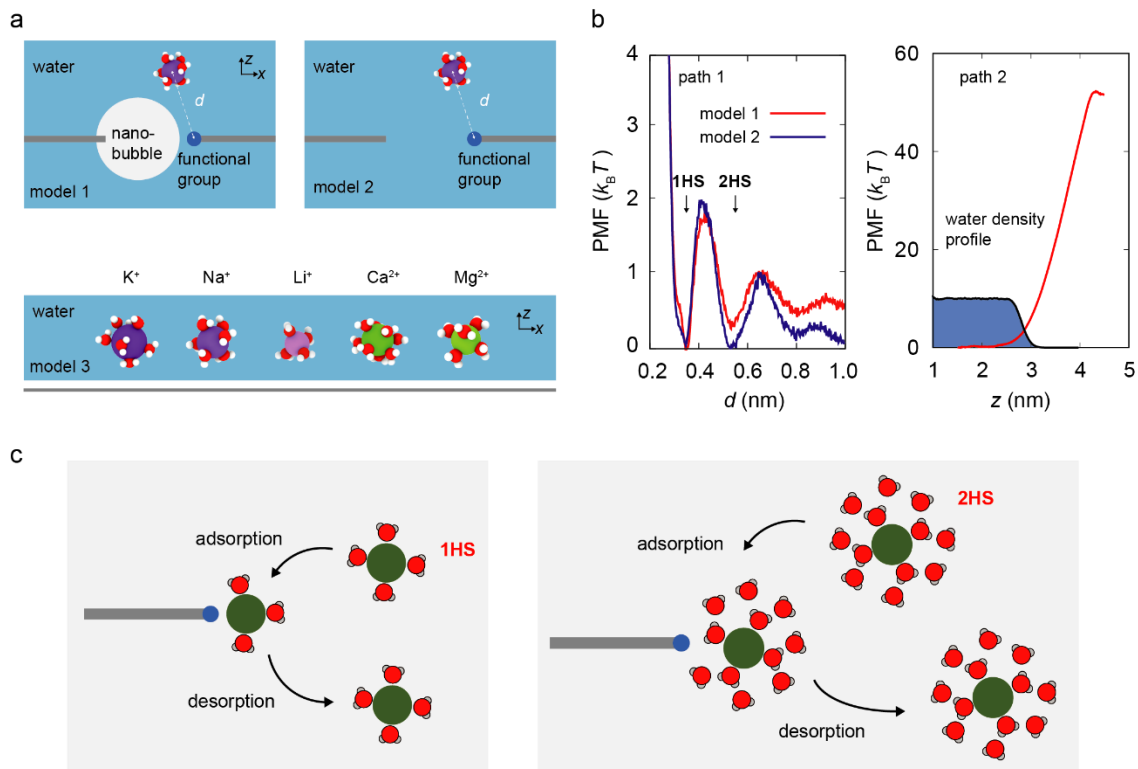
Figure S1. (a) Illustration of molecular simulation models: Models 1 and 2 for the PMF of ions translocated with hydration shells perturbed by the functionalized graphene edges, which are coated by a thin water film or immersed in water, respectively. Model 3 for the calculation of hydration radii of ions. (b) PMF profiles for path 1 (models 1 and 2) and path 2. (c) Illustration of the adsorption-desorption process of ion translocation through the thin water layer, with the 1st or 2nd hydration shells (1HS/2HS) perturbed by the functional groups.
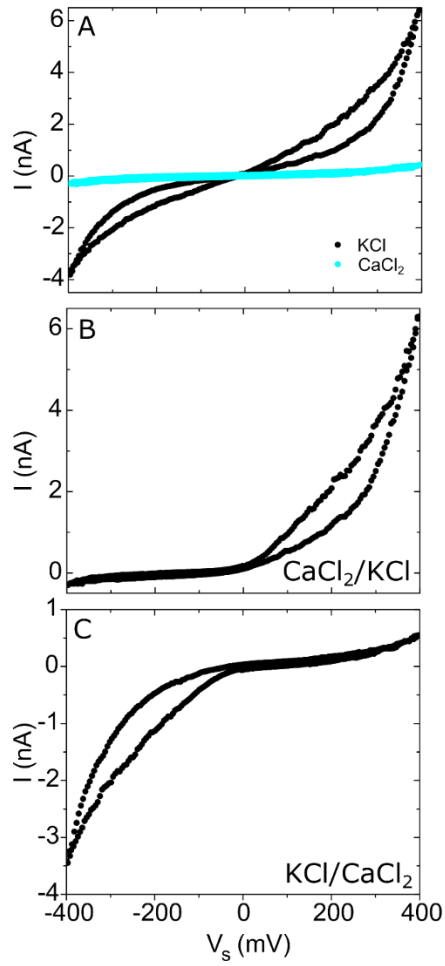
Fig. S2. Conductance under asymmetric ion conditions. (A) Symmetric ion conditions for both KCl and CaCl₂ at 0.1M chloride concentration. (B), (C) Asymmetric ion conditions in 0.1M chloride concentration.
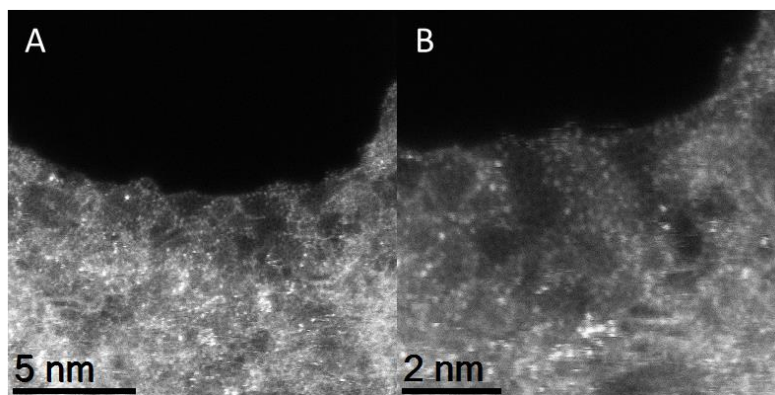
Fig. S3. Pore termination. Aberration-corrected medium-angle annular dark-field (MAADF) STEM images of CVD graphene (A) HIM drilled pore periphery, (B) HIM drilled pore edge showing nanopore geometry, edge structure, and hydrocarbon contamination.
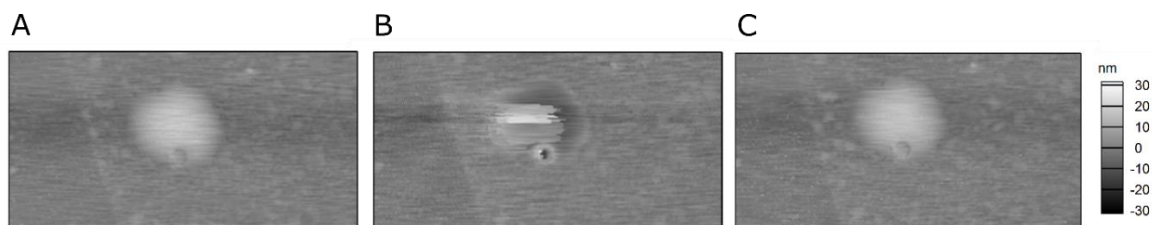
Figure S4. AFM images of the pore taken in water with different set point ratios of (A) 36%, (B) 30%, and (C) 36% again. The lower set point ratio increases tip-sample forces, which deform the bubble.
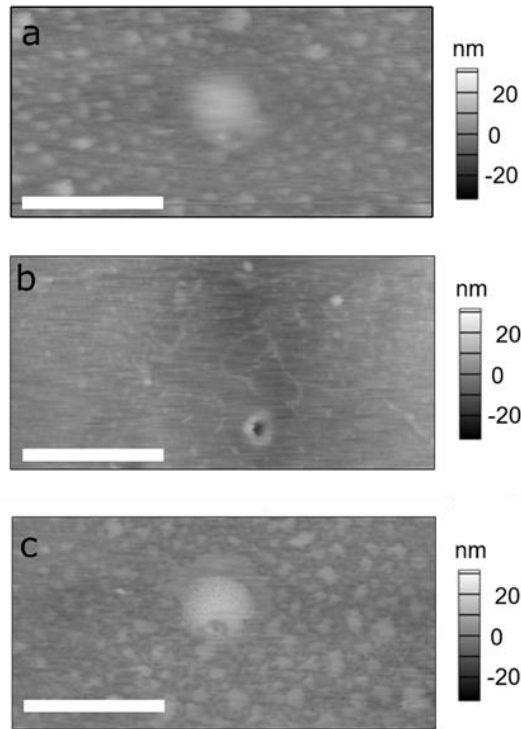
Figure S5. Pore Wettability. An ethanol/water exchange was monitored via liquid AFM imaging: (A) graphene pore in water with a surface nanobubble, (B) pore in ethanol solution with no surface nanobubble, and (C) the nanobubble returns when solution is exchanged back to water. Scale bars = 500 nm
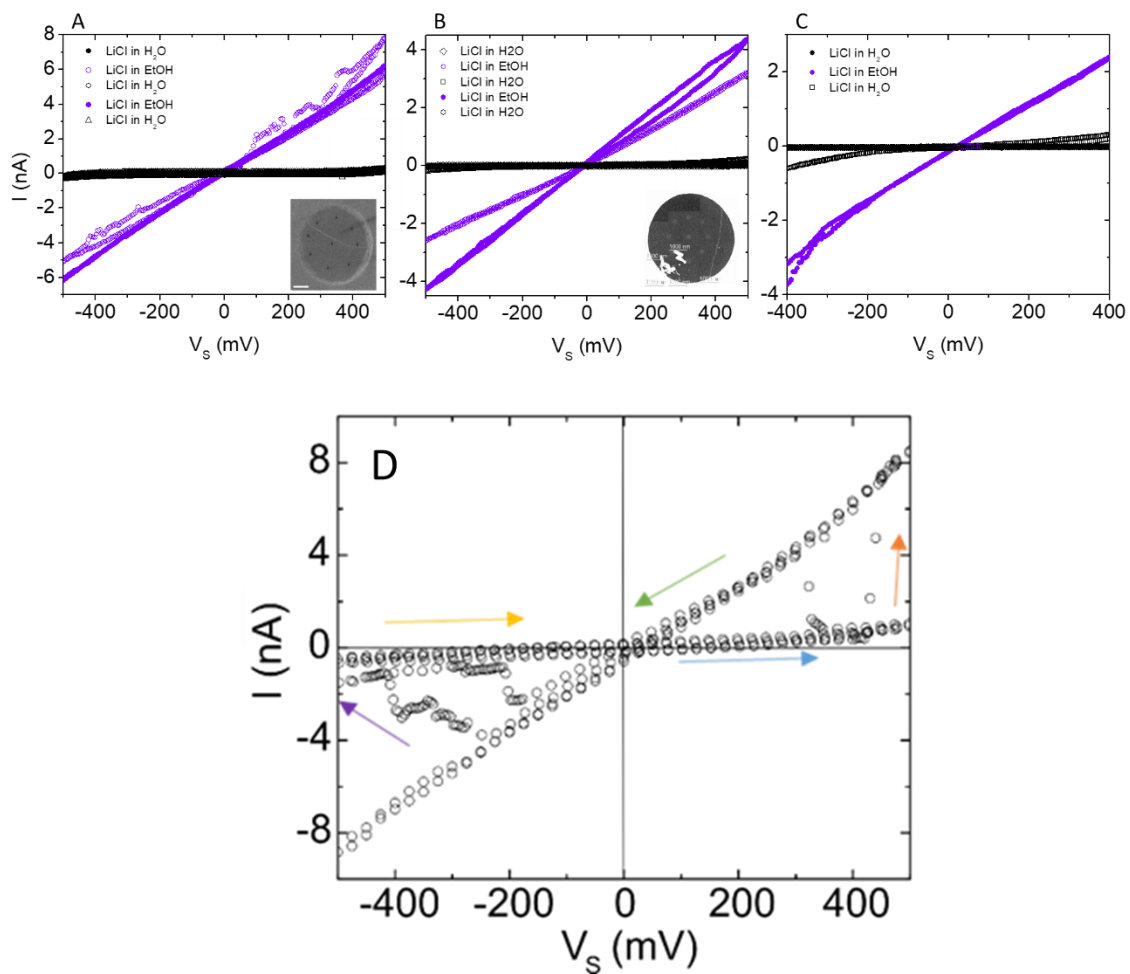
Fig. S6. Conductance in solutions of different surface tension. . (A-C) Aqueous and ethanol based 0.1M LiCl conductance across graphene nanopore device. Inset depicts (A)HIM and (B) STEM image of the device measured. Scale bar = 1 micron. Measurements are carried out in the order shown in the legend. The conductance of the LiCl in ethanol was greater than that of LiCl in water. (D) In situ measurement of conductance while switching between water and ethanol based 0.1M LiCl solutions.
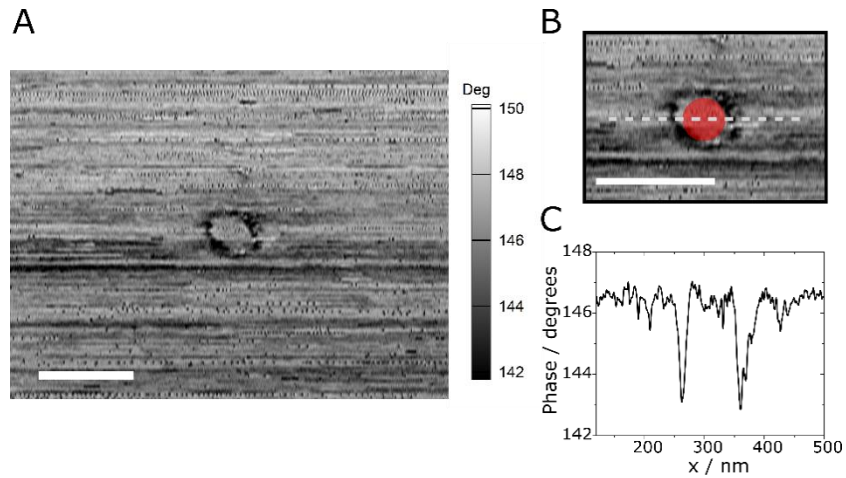
Figure S7. AFM imaging of non-occluded nanopore. A) AFM phase channel image of a HIM drilled nanopore. B) Expanded view of nanopore, with a comparison to the 75 nm circular pore implied by our conductance data. C) Phase line-cut across the pore (as shown in B) showing the outline of the pore. Scale bars are 200 nm.
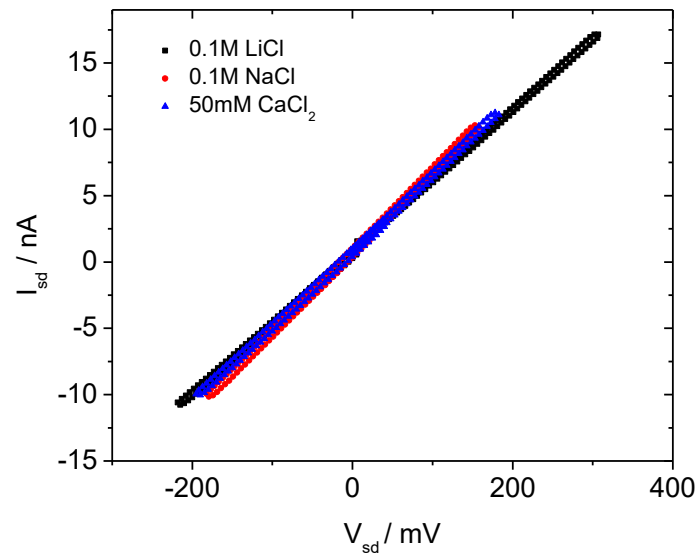
Figure S8. Two terminal I-V curves of the pore for different salts, taken immediately prior to the AFM measurements.
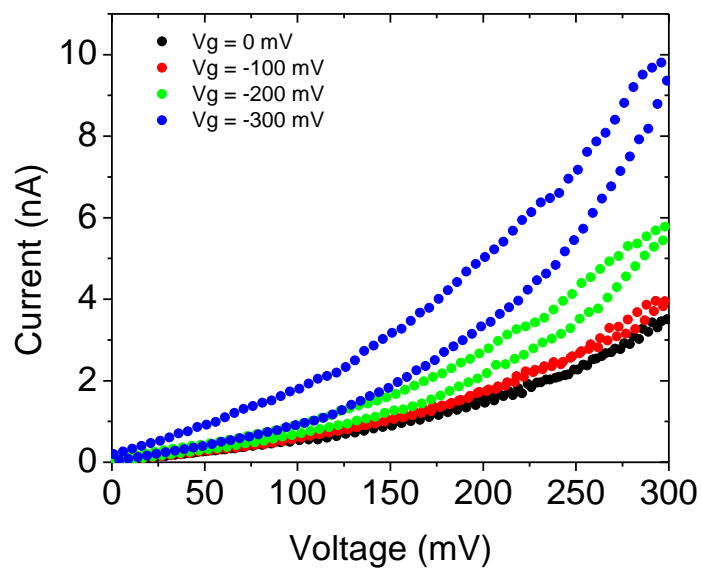
Figure S9. Typical hysteresis observed from applied gate voltage while sweeping source/drain

voltage from 0 mV to 300 mV and back down to 0mV, in a 0.1 M KCl concentration solution.
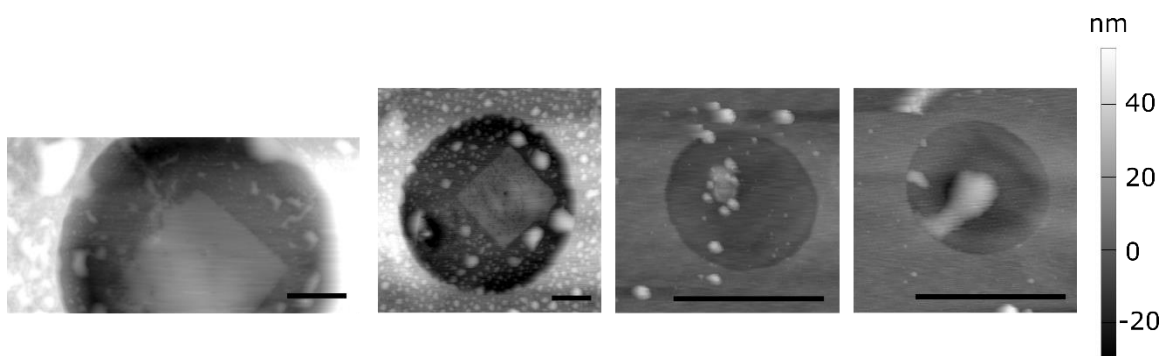
Figure S10. Examples of other devices we imaged which are covered in nanobubbles. The

devices were measured with AFM in water. Scale bars are 1µm.
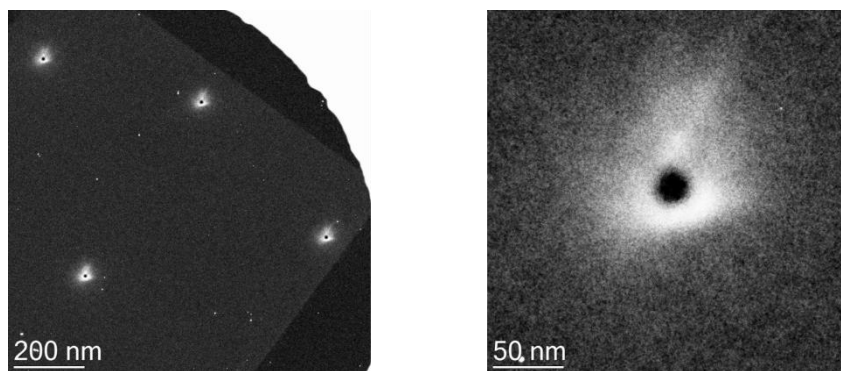
Figure S11. Evidence of hydrocarbon contamination around the nanopore mouth after HIM milling. The white region indicates charging is occurring on the electrically insulating hydrocarbon layer.

Ions	ε (kcal/mol)	σ (nm)
Na^+	0.02639	0.25907
K^+	0.12693	0.29988
Li^+	0.00274	0.22415
Ca^{2+}	0.09788	0.29132
Mg^{2+}	0.01020	0.24232

Tables S1. 12-6 Lennard-Jones (L-J) potential parameters used for the ions studied[6].

Salt solution	Bulk Conductivity (S/m)	Pore Conductance (nS)	Estimated pore size (nm)
100 mM LiCl	0.814	59.4	73.0
100 mM NaCl	0.884	65.7	74.3
50mM CaCl$_2$	0.834	62.3	74.7

Table S2. Bulk conductivities for each salt solution were measured prior to our experiments. The pore conductance was calculated from the data in Fig. S7, and was used with Eq. S1 to estimate the pore size.

References

1. S. Plimpton, Fast Parallel Algorithms for Short-Range Molecular Dynamics, *J. Comput. Phys.*, 1995, **5**, 10597.
2. N. Wei, C. Lv and Z. Xu, Wetting of Graphene Oxide: A Molecular Dynamics Study, *Langmuir*, 2014 **30** (12), 1-19.
3. P. Li, L. F. Song and K. M. Merz Jr., Systematic Parameterization of Monovalent Ions Employing the Nonbonded Model, *J. Chem. Theroy Comput.*, 2015 **11**(4), 1645-1657.
4. J. D. Weeks, D. Chandler and H. C. Anderson, Role of Repulsive Forces in Determining the Equilibrium Structure of Simple Liquids, *J. Chem. Phys.* 1971, **54**(12), 5237-5247.
5. B. Roux, The Calculation of the Potential Mean Force Using Computer Simulations, *Comput. Phys. Commun.*, 1995 **91**(1-3), 275-282.
6. N. Wei, C. Lv and Z. Xu, Wetting of Graphene Oxide: A Molecular Dynamics Study, *Langmuir*, 2014 **30**(12), 1-19.
7. A. Grossfield, *Wham: The Weighted Histogram Anaysis Method. Version 20.6*, (accessed 2018), http://membrane.urmc.rochester.edu/conent/wham.
8. K. Zhou and Z. Xu, Renormalization of Ionic Solvation Shells in Nanochannels, *ACS Appl. Mater. Interfaces*, 2018 **10**(33), 27801-27809.
9. Eslami B, Solares S D (2017) Imaging of surface nanobubbles by atomic force microscopy in liquids: Influence of drive frequency on the characterization of ultrasoft matter. *Microscopy Research and Technique*. **80**:41-49.
10. H. An, B. H. Tan, and C.-L. Ohl, Distinguishing Nanobubbles from Nanodroplets with AFM: The influence of vertical and lateral imaging forces, *Langmuir*, 2016 **32**(48), 12710-12715.
11. Adamson A W, Gast A P (1997) *Physical chemistry of surfaces* (6th ed.). Wiley.
12. Hafiz-ur-Rehman, Shahid A M (2008) Density, Viscosity, and electrical conductivity measurements on the ternary system $H_2O + C_2H_5OH + LiCl$ over the entire ranges of solvent composition and LiCl Solubility from (-5 to +50) ^{o}C. *J. Chem. Eng Data*, **53**(9):2072-2088.
13. Garaj S, Hubbard W, Reina A, Kong J, Branton D, Golovchenko J A (2010) Graphene as a subnanometre trans-electrode membrane. *Nature* **467**:190-193.